aerospace

MDPI

Article

Multi-Fidelity Modelling of the Effect of Combustor Traverse on High-Pressure Turbine Temperatures

Mario Carta [1,*], Shahrokh Shahpar [2], Tiziano Ghisu [1] and Fabio Licheri [1]

[1] Department of Mechanical, Chemical and Materials Engineering, University of Cagliari, 09123 Cagliari, Italy; t.ghisu@unica.it (T.G.); fabio.licheri@unica.it (F.L.)
[2] Rolls-Royce Plc, Fluid Mechanics, Derby DE24 8BJ, UK; shahrokh.shahpar@rolls-royce.com
* Correspondence: mario.carta@unica.it

Abstract: As turbine entry temperatures of modern jet engines continue to increase, additional thermal stresses are introduced onto the high-pressure turbine rotors, which are already burdened by substantial levels of centrifugal and gas loads. Usually, for modern turbofan engines, the temperature distribution upstream of the high-pressure stator is characterized by a series of high-temperature regions, determined by the circumferential arrangement of the combustor burners. The position of these high-temperature regions, both radially and circumferentially in relation to the high-pressure stator arrangement, can have a strong impact on their subsequent migration through the high-pressure stage. Therefore, for a given amount of thermal power entering the turbine, a significant reduction in maximum rotor temperatures can be achieved by adjusting the inlet temperature distribution. This paper is aimed at mitigating the maximum surface temperatures on a high-pressure turbine rotor from a modern commercial turbofan engine by conducting a parametric analysis and optimization of the inlet temperature field. The parameters considered for this study are the circumferential position of the high-temperature spots, and the overall bias of the temperature distribution in the radial direction. High-fidelity unsteady (phase-lag) and conjugate heat transfer simulations are performed to evaluate the effects of inlet clocking and radial bias on rotor metal temperatures. The optimized inlet distribution achieved a 100 K reduction in peak high-pressure rotor temperatures and 7.5% lower peak temperatures on the high-pressure stator vanes. Furthermore, the optimized temperature distribution is also characterized by a significantly more uniform heat load allocation on the stator vanes, when compared to the baseline one.

Keywords: jet engine; hot streak migration; conjugate heat transfer; phase-lag simulation

check for updates

Citation: Carta, M.; Shahpar, S.; Ghisu, T.; Licheri, F. Multi-Fidelity Modelling of the Effect of Combustor Traverse on High-Pressure Turbine Temperatures. *Aerospace* **2024**, *11*, 750. https://doi.org/10.3390/aerospace11090750

Academic Editor: Sergey Leonov

Received: 25 July 2024
Revised: 3 September 2024
Accepted: 10 September 2024
Published: 12 September 2024

Copyright: © 2024 by the authors. Licensee MDPI, Basel, Switzerland. This article is an open access article distributed under the terms and conditions of the Creative Commons Attribution (CC BY) license (https://creativecommons.org/licenses/by/4.0/).

1. Introduction

The continuous striving for higher engine cycle efficiencies has led the high-pressure turbines (HPT) of modern turbofan engines to experience increasingly high temperatures [1]. During decades of research and experimentation, many systems have been devised to shield the HPT blades from the extreme heat carried by the combustion gases. These include thermal barrier coating, refrigerant injection from the hub and casing cavities, in addition to highly sophisticated internal and external film cooling [2,3]. The combined action of these and other countermeasures works to protect the metal alloy, the melting point of which is usually around 1400 K [4], from gas currents impinging on the blades with temperatures of 1800–2000 K and beyond [5,6]. Film cooling is also used on the turbine end-walls [7–9].

In many cases, due to the can-type arrangement and cooling, the temperature distribution delivered by the combustor is characterized by a circumferential alternance of high- and low-temperature regions. As a result, a circular array of high-temperature streams, commonly known as "combustor hot streaks", migrates through the HPT stage and interacts with the blades [10]. Typically, these streams will have twice the average free-stream stagnation temperature and have been found to cause a significant (10–30%)

increase in HPT rotor heat load [11]. Due to the high rotational speed and gas pressure, the rotor's structure is already highly loaded [12], hence the thermal stress resulting from the interaction with these hot streaks represents an additional burden on the rotor. Local overheating of the rotor structure can lead to faster creep [13] and deterioration of the metal on a microstructural level [14,15], hindering its ability to withstand future mechanical stress. This can result in a severe reduction of the blade's service life as indicated by Han et al. [16]. The blade's surface promotes oxidation and hot corrosion processes [17,18] that have been shown to cause extensive aerodynamic losses [19,20]. Therefore, designers must pay particular attention to the absolute values and distribution of the rotor surface temperatures, ensuring that the critical regions are properly covered by film cooling.

In terms of temperature distribution, it is a known fact that, due to their higher streamwise velocity and crossflow vorticity, combustor hot streaks approach the rotor with an incidence angle that is larger than the one of the surrounding flow. This causes them to predominantly impinge on the pressure surface of the blade, rather than the suction surface [21]. This phenomenon, which was observed experimentally by Butler et al. [22], is known as the Kerrebrock–Mikolajczak effect [23] or hot/cold gas segregation. Based on the experimental conditions adopted by Butler in [22], Rai and Dring [24] conducted a two-dimensional computational study on a turbine case, emphasizing the significant temperature excursions and segregation effects experienced by the HP rotor in the presence of hot streaks. Three-dimensional studies were later conducted by Dorney et al. [25] and Takahashi and Ni [26] on the same case, both achieving better agreement with experimental data. These studies highlighted the importance of capturing the migration's spanwise components within the rotor passage. For example, as shown by Dorney et al. in [27], the evolution of the hot streaks is affected by the tip clearance size, which is found to promote a radial spreading of the hot flow currents. Tip clearance can also affect the amount of over-tip leakage (OTL) flow, which is known to increase the local heat transfer rates [28–30].

Clearly, the initial spanwise position of the hot streaks approaching the turbine is itself a key parameter. In some cases, the radial inlet temperature distribution, also called "traverse", can be characterized by a radial "bias", i.e., a profile that is unbalanced towards either the inner or outer radii. In most cases, the latter option is less desirable, as an increase in rotor heat load towards the tip is more difficult to counteract and can lead to faster deterioration rates and failure [31–33]. Migration patterns are highly influenced by modifications in the circumferential position of the hot streaks with respect to the stator vanes, which is often referred to as "clocking" of the temperature distribution. It is known that by positioning the hot streaks so that they directly impinge on the leading-edge area of the stator, the peak temperatures on the rotor can be mitigated at the cost of a higher heat load on the stator itself [34]. The existence of this trade-off was also confirmed by An et al. [35] who conducted a detailed numerical investigation on the effects of clocking on peak temperatures and heat load fluctuations on both stator and rotor blades. The clocking effect on the rotor heat load has also been found to be dependent on the hot streaks' circumferential wavelength, which is in turn dictated by the number of burners that characterize the combustor configuration [36]. Other studies by Zhang et al. [37] and Yang et al. [38] have assessed the impact of swirl angle and clocking on peak high-pressure stator heat load and hot streak interaction with the formation of secondary flows.

In terms of computational modelling, many different techniques have been employed in the past to simulate hot streak migration. These studies can provide important insights into the impact of the model's fidelity on the accuracy of the results under different aspects. The RANS simulation technique in the work of Michelassi et al. [39] involved using a mixing-plane interface between the high-pressure stator and the rotor. In a similar fashion, but using the average passage approach introduced by Adamczyk [40], Turner et al. [41] adopted a steady-state RANS simulation with a k-ε turbulence closure. Although these investigations achieved a fairly good agreement with the experimental data, as Turner pointed out, a costly, full, unsteady simulation would be required to accurately model the wake splitting effect on the rotor. Praisner et al. [42] assessed the impact of different

turbulence modelling techniques for RANS simulations, concluding that the best results were achieved by adopting a k-ω model. Praisner also assessed the impact of steady versus unsteady modelling, arguing that the increased accuracy achieved with full-unsteady simulations was not significant enough to warrant the rise in computational cost. In the same work, the importance of using a realistic geometry when modelling this type of phenomenon was also highlighted.

In the present work, a parametric analysis on the effects of circumferential clocking and radial bias on hot streak migration and rotor surface temperatures was conducted. The case study is the high-pressure turbine from a modern commercial turbofan engine. Numerical investigations are carried out on a 1 ½ stage computational domain which includes the high-pressure stator, high-pressure rotor, and intermediate-pressure stator. Unsteady (phase-lag) RANS simulations are performed on six different combinations of clocking and radial bias values. To model rotor–stator interaction, phase-lag simulations such as the ones that have been used by the authors in [43] were performed on each case, capitalizing on the periodic nature of the inlet distribution to reduce computational cost. All the phase-lag cases were run using a "simplified" representation of the rotor geometry, where the blade is solid (non-hollow). For three cases out of a total six, specifically those pertaining to the different values of the radial bias parameter, steady-state conjugate heat transfer (CHT) simulations are also carried out on more realistic versions of the rotor geometries, which include the internal cavities and cooling holes. These CHT simulations are carried out in steady-state conditions only, due to the high computational cost. A similar approach was also followed by Deng et al. in [44]. The objective of running the CHT simulation was to assess whether the deltas in temperature predicted by the external models for the different bias configurations were still maintained, when adding the fidelity of modelling the fluid–solid thermal exchange in the rotor.

The purpose of this investigation is to provide insight into the effects of modifications in the turbine inlet temperature distribution on peak high-pressure stator and high-pressure rotor temperatures using high-fidelity simulations. Instead of performing this analysis on simplified test-cases, real geometries from modern commercial jet engines were used, with boundary conditions representative of real operating points of the machine.

This paper is organized as follows: the numerical setup, comprising the geometries, parametrized boundary conditions, meshing, and solving techniques utilized for the present analysis are discussed in the next section. The third section contains a comparative discussion of the numerical results obtained in the parametric analysis, with the identification of the best-performing inlet configuration among those studied. Leveraging the findings reported in the third section, a new inlet distribution is generated and tested, and the corresponding results are presented in the fourth section of this paper. The last section provides the concluding remarks.

2. Methodology

2.1. Geometry and Boundary Conditions

The computational domain used for the present analysis was a 1 ½ stage turbine, which included a high-pressure stator (HPS), a high-pressure rotor (HPR), and an intermediate-pressure stator (IPS). Simulations were run on two different models. In the external phase-lag cases, where the setup corresponded to the scheme of Figure 1A, a sliding-plane interface was used between the HPS and HPR domains. This allowed for circumferential variations in the flow conditions to be communicated through the first two rows. A mixing-plane interface was used between the HPR and the IPS, as the focus of the phase-lag analysis was to study the temperature distribution's migration through the high-pressure stage only. For the CHT simulations carried out on the model of Figure 1B, all the rows were connected through mixing-plane surfaces, being that only steady-state runs were performed on this setup. The CHT domain also included a solid HPR mesh, which exchanges heat with the fluid one. The HPS geometry contained a set of "RIDN" and "RODN" cooling-hole rows. These were placed at the inner and outer stator end-walls, respectively, upstream

of the vanes, as indicated in Figure 1. These cooling holes serve the function of providing refrigerant flow for the stator end-walls. For the external cases, film cooling on the stator and rotor blades was modelled using source terms in the form of "strip" models. These are indicated with dashed red lines in Figure 1A on both HPS and HPR. In the conjugate model (Figure 1B), the strip models were present on the HPS, but the HPR film cooling was simulated in high-fidelity by providing the coolant in an inlet at the root of the blade (FC in Figure 1B) and letting the coolant travel internally in the blade cavity and through the cooling holes while exchanging heat with the solid mesh. The IPS exit BC ("MAIN EXIT" in Figure 1) was a radial one-dimensional static pressure profile. In both models of Figure 1, simulations were run on single-passage HPR and IPS geometries by enforcing periodic boundaries at the domains' sides. The HPS periodic domain contained two complete airfoils to accommodate the entire circumferential variability, generated by the combustor, in the main inlet BC. The main HPS inlet boundary condition, indicated as "MAIN INLET" in Figure 1, is represented by a 2D field of total pressure, total temperature, flow angles, inlet turbulence quantities, and fuel mixture fraction.

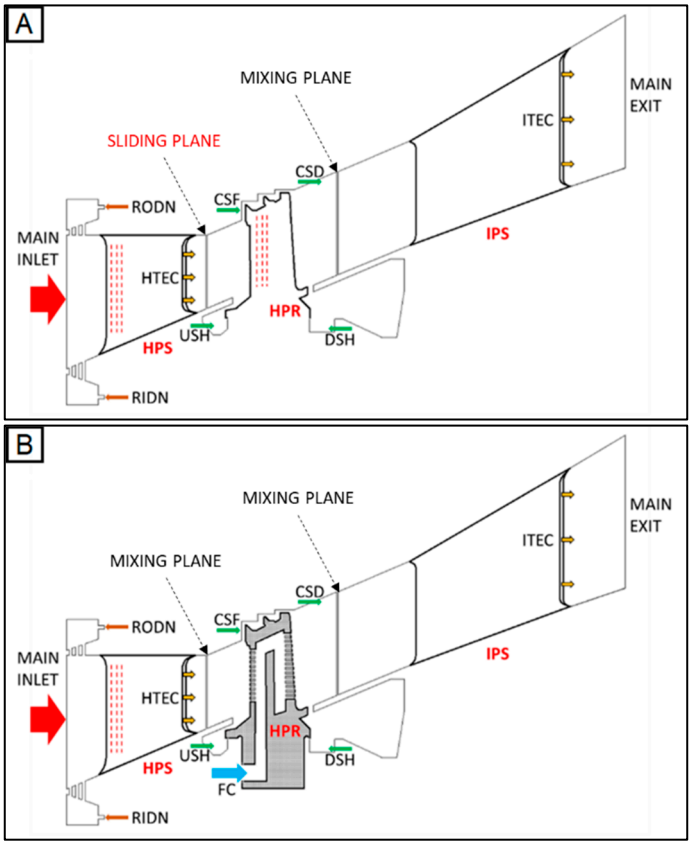

Figure 1. Schematic of the computational domain used for the "external" (**A**) and "conjugate" (**B**) flow simulations. Film cooling strip models are represented by the dashed red lines. The meaning of the acronyms can be found in nomenclature—picture distorted and not to scale.

The baseline boundary conditions being used for the present investigation are representative of the engine's maximum take-off operating point. The baseline total temperature field is represented in Figure 2A as case C0. The locations of the HPS leading edges are indicated within the figure by the dashed white lines. Starting from the baseline temperature field, the distribution is modified by acting on two parameters, namely "bias" and "clocking". The biasing is performed by adding a harmonic field (function or the radius) to the baseline temperature field, thus maintaining the original temperatures at the hub and at the tip, and acting on the core temperature distribution. This is followed by scaling to ensure that the mass-weighted integral of the biased temperature distribution (proportional

to the amount of energy contained in the inlet field) is the same for each case. In Figure 2A, the total temperature fields C1 and C2 present the effect of hub and casing bias, respectively.

Table 1. List of parametric inlet temperature field cases.

Clocking \ Bias	0°	θp/2
+10% span	CASE 2	CASE 5
0	CASE 0	CASE 3
−10% span	CASE 1	CASE 4

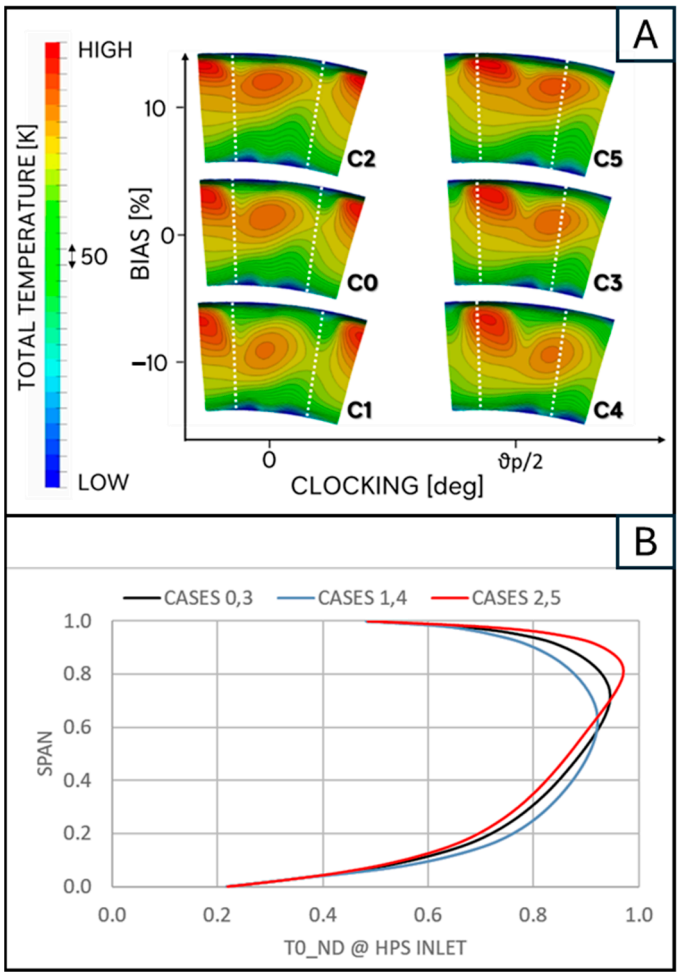

Figure 2. Total temperature contours at the HPS inlet corresponding to the different combinations of clocking and bias for the same cases listed in Table 1; the dashed white lines represent the HPS LE positions (**A**), and RTDs at the HPS main inlet for the different cases in terms of non-dimensional total temperatures $T0_{\_ND}$ as a function of span with original distribution in black, low bias in blue, and high bias in red (**B**).

The circumferentially averaged radial temperature distributions (RTD) are displayed in Figure 2B in terms of non-dimensional total temperature ($T0_{\_ND}$ = T0/Tref) as a function of span (where Tref is a reference temperature value that cannot be disclosed for industrial confidentiality reasons). The amount of bias applied to the distribution is such that the inlet temperature peak of the original RTD is shifted downwards or upwards by 10% of the span. This can be seen in Figure 2B. The clocking modification is applied by tangentially shifting the inlet distribution by half the HPS pitch angle ($\theta_p/2$). This causes the hot region, which is approximately halfway between the simulated vanes (cases C0, C1, C2) to be shifted in

front of the leading edges (cases C3, C4, C5). Table 1 presents a list of the different HPS inlet temperature distributions that have been generated for the purpose of this investigation.

2.2. CFD Meshing

This section describes the techniques employed to generate the three-dimensional computational grids used for this numerical analysis. As indicated in the previous section, two models are adopted for the purpose of this investigation, namely the external one (Figure 1A) and the conjugate one (Figure 1B). In both approaches, the computational meshes for the high-pressure domains (HPS, HPR) are unstructured hexa-dominant with 20 structured prismatic layers near the walls. These meshes are generated with BOXER [45]. The IPS domain mesh is a H-O-H multi-block structured grid, with 20 layers in the O-block. This hexahedral mesh is generated by PADRAM [46] which is a Rolls-Royce parametric design and rapid templated meshing tool. For all the meshes used, cell height first was set to achieve a y^+ of 1 or below on all the walls.

The mesh densities were chosen as a result of a mesh independence study, which was presented in [43] for the same 1 ½ stage computational domain. During meshing, refinement techniques were used to increase grid density in critical areas such as the RIDN and RODN tubes in the HPS domain, trailing edges, cooling slots (HTEC, ITEC in Figure 1) and the rotor tip geometry. Volume-refinement shells were used to improve the mesh density and quality in the wake regions on all the blade rows. A view of the HPS mesh is displayed in Figure 3A with a close-up on the hub region where the RIDN holes can be observed. The HPS and HPR BOXER meshes had a cell count of 25 million and 35 million, respectively. The IPS mesh, generated in PADRAM, had a number of elements of around 3.4 million.

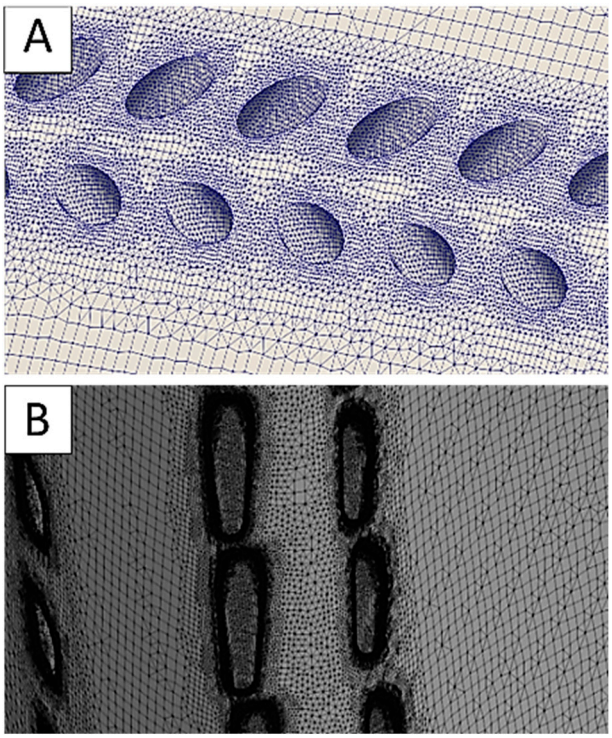

Figure 3. Close-up views of the computational grid over the stator hub showing RIDN holes (**A**) and view of the mesh of the rotor blade surface of the conjugate model with the LE cooling hole rows on display (**B**)—pictures distorted.

For the conjugate model (Figure 1B), the 1 ½ stage domain used the same stator meshes (HPS, IPS) of the external model. The conjugate HPR domain, to be used in the CHT simulations, is meshed in BOXER and, as previously mentioned, includes fluid and

solid sub-domains. These meshes are generated simultaneously in a single BOXER run, thus ensuring a conformal interface between the fluid and solid grids. The fully featured rotor mesh presents 22 prismatic layers on all the surfaces, with the same first cell height adopted for the external model, ensuring a y+ of 1. The conjugate HPR mesh required significantly finer refinement with respect to the external one, due to the presence of various small-scale geometrical features such as ribs in the internal cavity of the mesh and the cooling holes. Particularly high levels of mesh refinement are applied in proximity of the edges of the cooling holes. The resulting significant increase in local mesh density is visible in Figure 3B. The same refinement was imposed on the opposite ends of the cooling holes, where they overlook the internal cavity of the HPR blade. The cell counts of the conjugate HPR fluid and solid meshes were, respectively, of 190 million and 60 million. For more details on the meshing technique adopted for this part of the work, the reader can refer to [43].

2.3. Numerical Simulation Technique

The software used to perform all the simulations in the present work was HYDRA [47], which is a proprietary Rolls-Royce unstructured, density-based CFD solver with unsteady and conjugate heat transfer capabilities. The full 3D Reynolds-Averaged Navier-Stokes (RANS) equations were solved with an implicit single-grid scheme. The k-ω Shear Stress Transport (SST) model was adopted for the RANS turbulence closure. A CFL number of 20 was used for the time-marching scheme for all the simulations. In the external phase-lag simulations of the model of Figure 1A, steady-state runs were initially performed to provide good initial solutions for the subsequent phase-lag simulations. The convergence criterion for all the simulations was achieved when the residual values dropped under a threshold of 10^{-11} for all the equations.

The phase-lag simulation technique makes use of a combination of harmonic terms to represent the periodic unsteadiness characterizing stator-rotor interaction. Further details on the implementation of this technique can be found in [48,49]. For the present work, phase-lag simulations were run for 10 cycles to achieve a good stabilization of the cyclical variability of the quantities of interest. The last cycle (n. 10) of each phase-lag simulation was finally post-processed to obtain the flow-fields and metrics of interest, both instantaneous and cycle-averaged. In the present analysis, six harmonics were used to transmit the periodic variability at the HPS–HPR interface. Each cycle was articulated into 363 time-steps, with ten internal iterations per each time-step. This number of sub-iterations allowed us to achieve the 10^{-11} convergence criterion for the individual time step. Monitors were placed onto the HPS and HPR surfaces to gather data on the unsteady forces exchanged by these blades with the flow. These monitors were used to assess the level of convergence of the phase-lag calculation. This was determined in real time by calculating the difference between the previous cycle's computed force at the same phase, and the one for the current cycle. These error metrics are shown in Figure 4A (stator force error) and Figure 4B (rotor force error), where it can be seen that the difference becomes gradually smaller as the phase-lag calculation progresses. This indicates that the time-periodicity of the flow-fields' behavior was being achieved gradually. The calculations were stopped once the phase-to-phase difference in HPR force from the previous cycle remained within 2% for a whole period.

For the CHT simulations on the domain of Figure 1B, while solving the steady-state RANS equations in the fluid domain, a multigrid explicit scheme was tasked with solving the heat conduction equation inside the solid domain. Heat was transferred between the two domains at the conformal interface every 10 iterations. The numerical techniques used for the purpose of this analysis were the same as those used by the authors in [43], where the reader will be able to find a more detailed description of the methodology. This also includes a validation study where the predictions of the models used in the present work were compared against experimental data.

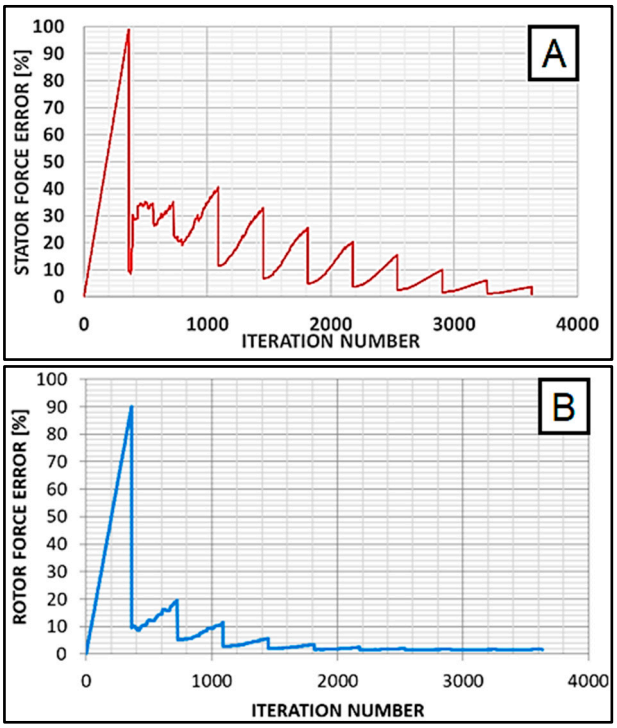

Figure 4. Convergence of the phase-lag simulation in terms of stator force error (**A**) and rotor force error (**B**) monitored during the iterative calculation process.

3. Results and Discussion

This part of the work presents the results obtained via phase-lag and CHT simulations on the different cases listed in Table 1. A preliminary analysis was conducted on the baseline case (CASE 0) to locate the main flow phenomena and the critical regions on the blade that will constitute the focal point of the comparative analysis. Figure 5 shows the instantaneous static temperature contours for a mid-span section of the HPS and HPR domains. As previously mentioned, the domains have different sizes in the circumferential direction due to the different periodicity angle and the fact that the HPS domain houses two complete airfoils. It can be seen from Figure 5 how the phase-lag simulation allows for the circumferential variability of the flow-field to be transmitted through the sliding plane (see Figure 1A). In particular, the instantaneous contours of Figure 5A capture the migration of the hot region visible in Figure 2A for case 0 at the top-right corner of the inlet patch. Figure 5B shows instantaneous static temperature contours on the midspan section of the HPR row.

The effects of the segregation effect can be seen on the rotor, where the gas streams with higher temperature only impinge on the leading-edge pressure-side (LE-PS) region of the blade while the suction side (SS) and trailing edge (TE) of the blade only come in contact with relatively cold flow streams throughout the cycle.

To study the cycle-averaged near-wall gas static temperatures experienced by the HPR along the span, the domain was sectioned at three span sections corresponding to 25%, 50%, and 75% spans. Surface static temperatures were then plotted as a function of a curvilinear co-ordinate (CC) going around the blade from TE to the LE through the PS, and back to the TE through the SS. This representation is shown in Figure 6. For the "baseline" conditions corresponding to case C0, the critical region on the HPR blade in terms of peak near-wall gas static temperatures can be identified with the LE region at 75% span (orange curve), at a curvilinear co-ordinate CC ≈ 0, followed by the mid-chord PS region ($-70 < CC < -30$). Since the objective of this study was to find the optimal inlet distribution capable of mitigating the peak near-wall gas temperatures on the HPR surface, these regions at 75% span will be the primary focus when comparing the various cases.

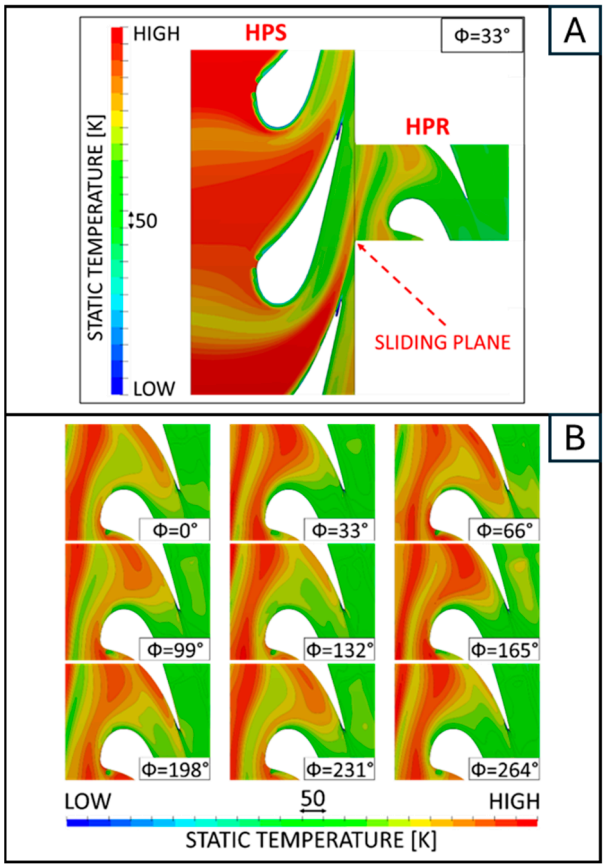

Figure 5. External phase-lag CFD, case 0 (baseline) instantaneous HPS and HPR static temperature contours at a mid-span section at cycle phase Φ = 33° with a view over the HPS–HPR sliding plane (**A**) and External Phase-lag CFD, case 0 (baseline) instantaneous HPR static temperature contours at a mid-span section at different period phases Φ (**B**)—Pictures distorted.

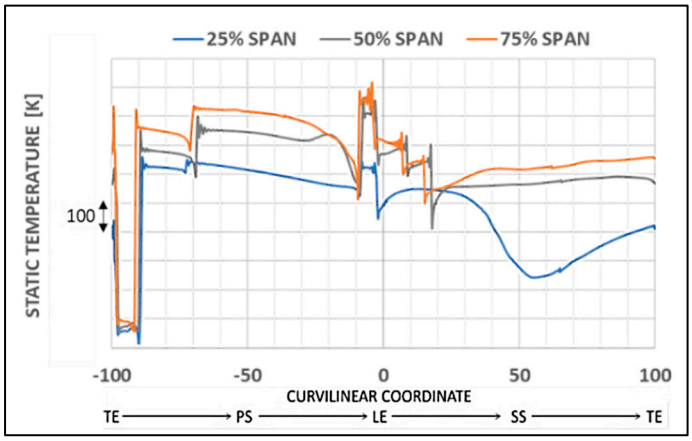

Figure 6. External phase-lag CFD, case 0 (baseline), near-wall gas static temperatures at three constant-span sections along the HPR blade height: 25% (blue), 50% (grey), and 75% (orange) resulting from cycle-averaged solutions, plotted as a function of the section's curvilinear co-ordinate.

3.1. Effect of Radial Bias

In this section, the effects of radial bias on the traverse migration patterns are assessed. Figure 7 reports the cycle-averaged, tangentially averaged RTDs at the exit of the stator row (Figure 7A) and of the rotor (Figure 7B) for cases 0, 1, and 2. As expected, migration of the flatter traverse case (case 1, blue curve in Figure 7) which has the same inlet energy content as the other cases, results in a significantly lower temperature profile in the critical region

(around 75% span) while it is characterized by moderately higher temperatures throughout the first half of the span.

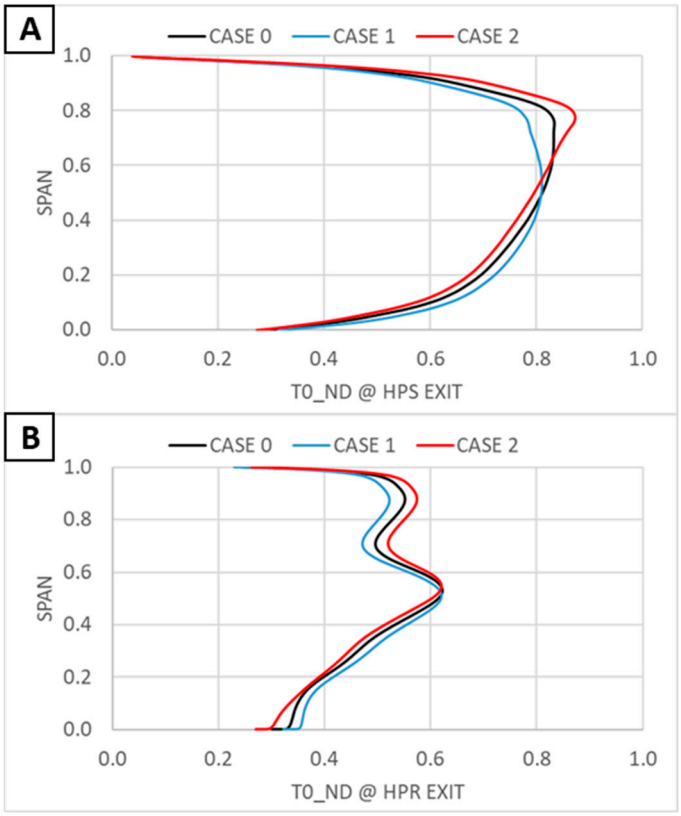

Figure 7. External phase-lag CFD, non-dimensional RTDs for case 0 (no bias, black), case 1 (negative bias, blue), and case 2 (positive bias, red) downstream of HPS (**A**) and downstream of HPR (**B**) resulting from cycle-averaged solutions, plotted as a function of blade span. Refer to Figure 1A for the locations of the RTDs.

Figure 8 shows the near-wall gas static temperature values on the HPR surface at different span sections. As shown in Figure 8, by adopting a flatter, negatively biased traverse (case 1) a ~50 K peak temperature reduction can be achieved in the LE region at a span of 75%, followed by a smaller reduction (~30 K) in the LE-PS region. This tendency is inverted at the lower span sections, especially at 25% span where the negative-bias case appears to provide an almost constant positive temperature offset at around 40 K. As mentioned before, the benefits of a temperature reduction in the top third of the blade outweigh an opposite-sign effect in the lower part.

To evaluate whether these significant temperature differences were still present when the fluid-solid thermal exchange was modelled, the same comparison was carried out for the CHT simulations. The results for the same three constant-span sections are shown in Figure 9 in terms of metal surface temperatures as a function of each section's curvilinear co-ordinate. The curves of Figure 9 show that the same tendency that was previously observed for the external phase-lag CFD simulations is also predicted by steady-state CHT, although with slightly smaller temperature deltas. In particular, the negative-bias traverse provides a reduction of peak metal temperatures of 20–30 K in the previously mentioned critical LE-PS region, which can be observed in the top graph of Figure 9 (75% span). Once more, the adoption of the negatively biased traverse appears to promote a similar amount of variation, but with opposite sign, throughout the lower section, with moderate temperature increases registered at the mid-span position. It is interesting to note that the 75% span surface temperatures are relatively less influenced by the same amount of positive inlet field biasing (red curve in Figure 9).

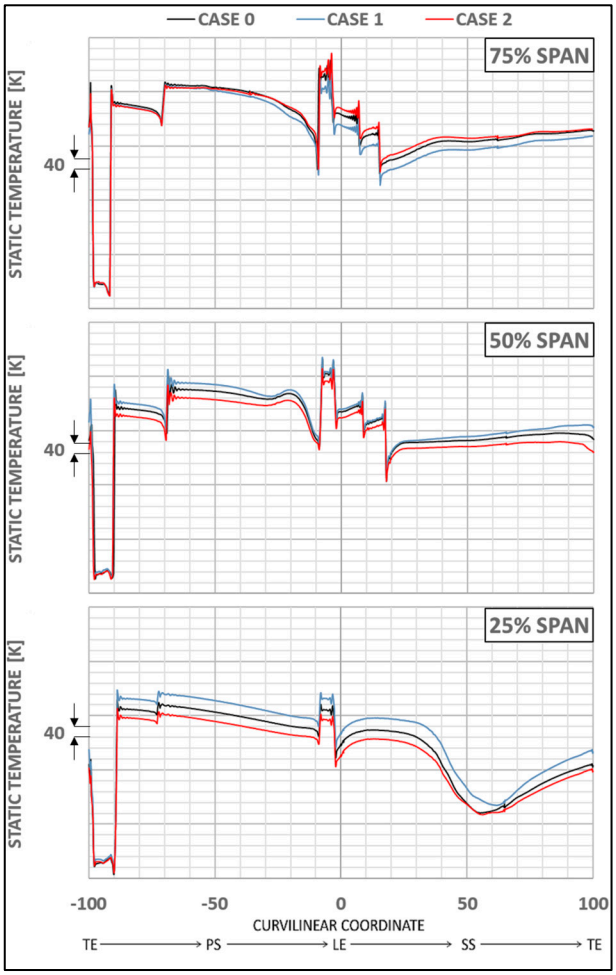

Figure 8. External CFD, near-wall gas static temperatures on the HPR surface for case 0 (no bias, black), case 1 (negative bias, blue), and case 2 (positive bias, red) at three constant-span sections resulting from phase-lag cycle-averaged solutions, plotted as a function of the section's curvilinear co-ordinate.

In other words, keeping the focus on the HPR critical region, the design under study appears to be robust with respect to tip (positive) traverse biasing, and more intensely reactive to hub (negative) traverse biasing, for the current operating conditions, both of which are clearly desirable features. As previously shown by the authors in [43], taking the unsteady stator–rotor interaction into account can have significant effects on HPR near-wall gas temperatures.

While it is self-evident that being able to transfer the circumferential variability at the HPS–HPR interface is vital to study clocking, it is interesting to assess whether the same is true when the analysis is focused on radial bias. In Figure 10, a comparison between the steady-state and phase-lag solutions is displayed for the 75% span section for the three bias values. The Figure shows that, while peak LE temperatures appear to be unaffected, the steady-state and phase-lag models predict remarkably different temperatures throughout the PS of the blade section. On the one hand, this means that even the current steady-state CHT simulations can provide meaningful results on global (LE @ 75% span) peak HPR temperatures, which are the primary focus of the present investigation. On the other hand, it is evident that excluding this unsteady interaction in the model will result in significant loss of accuracy (large underestimation) on the temperature predictions for the PS region of the blade. It is also worth noting that, although the steady-state temperature values themselves are sometimes off by more than 120 K, the deltas due to bias predicted by the

steady state model between the cases shown in Figure 10 appear to be roughly in agreement with the phase-lag ones.

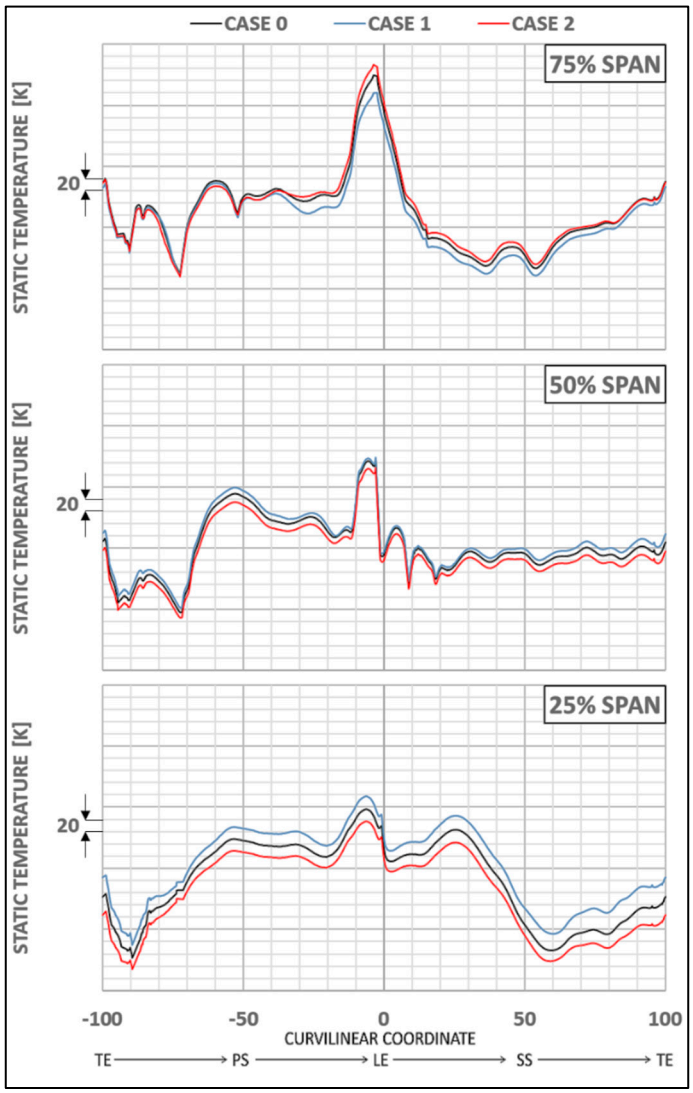

Figure 9. Conjugate heat transfer simulations, static temperatures on the HPR metal surface for case 0 (no bias, black), case 1 (negative bias, blue) and case 2 (positive bias, red) at three constant-span sections resulting from steady-state solutions, plotted as a function of the section's curvilinear co-ordinate.

3.2. Effect of Circumferential Clocking

In this section, the effects of inlet traverse clocking on surface temperatures are discussed. Figure 11 shows the HPR near-wall gas static temperatures, focusing on the critical (75%) span section for the different cases. The curves in black indicate the response to the zero-clocking traverse, while the cases in green pertain to the half-pitch clocking cases. Each plot in Figure 11 compares the two curves for a given radial bias value. To enhance the visibility of the delta between the two sets of curves in the relevant parts of the section, the lower limit of the vertical (temperature) axis has been increased. As a result of this, a small portion of the curves in the TE-PS region (CC ≈ -95) is excluded from the representation. The missing portion of the section did not add any useful information, as the two sets of curves appeared to be superimposed. This is due to the prevalent effect of the TE film cooling strip model, locally imposing the same near-wall gas temperature equal to the coolant temperature, regardless of the choice of inlet temperature distribution.

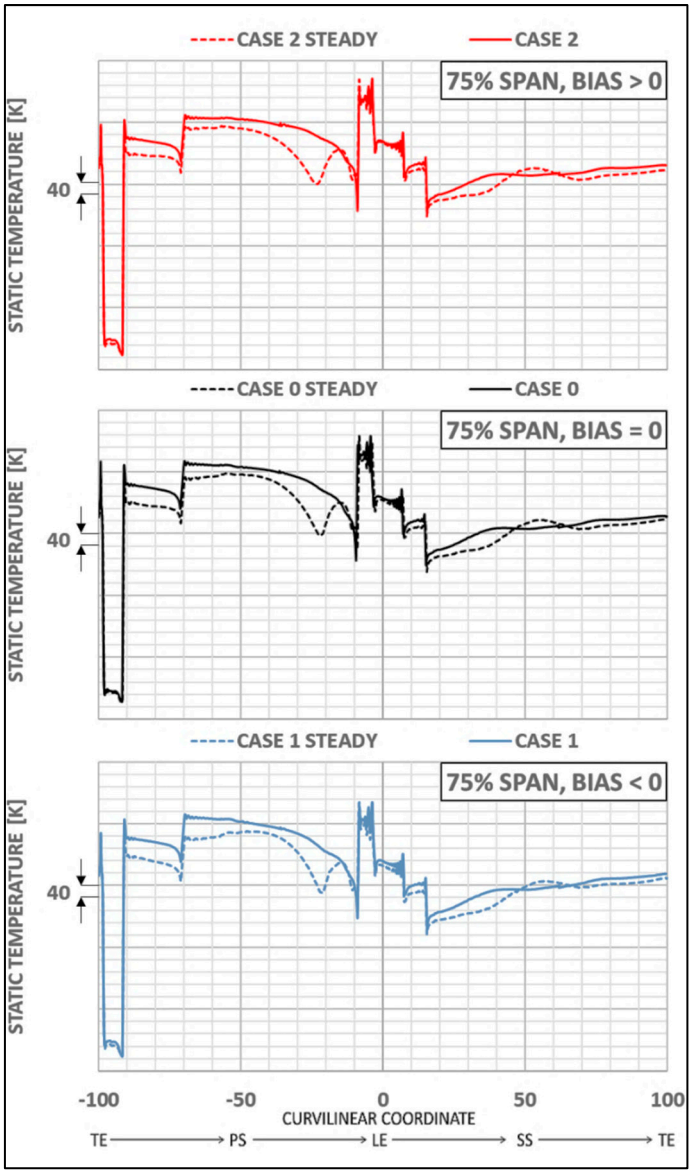

Figure 10. External CFD, near-wall gas static temperatures on the HPR surface for case 0 (no bias, black), case 1 (negative bias, blue) and case 2 (positive bias, red) at three constant-span sections resulting from steady-state solutions (dashed curves) and phase-lag cycle-averaged solutions (solid curves), plotted as a function of the section's curvilinear co-ordinate.

By observing the plots of Figure 11 and comparing them with the data presented in the previous section, it can be noted that the effects of a half-pitch clocking are less pronounced than those due to bias on HPR near-wall gas temperatures. For the positive 10% bias case (the top graph in Figure 11), the adoption of a half-pitch-clocked inlet temperature distribution appears to mitigate the negative effects introduced by tip biasing, with a reduction in static temperature at the LE of about 10–15 K and a larger reduction (about 20 K) in the PS region. In the no-bias and negative-bias cases (middle and bottom graphs in Figure 11), clocking results in slightly (5–10 K) lower PS temperatures at the expense of higher (10–20 K) SS temperatures with no significant peak (LE) variations. Although the effects of clocking seem to be of moderate entity on the HPR peak surface temperatures, the same cannot be said for the HPS ones.

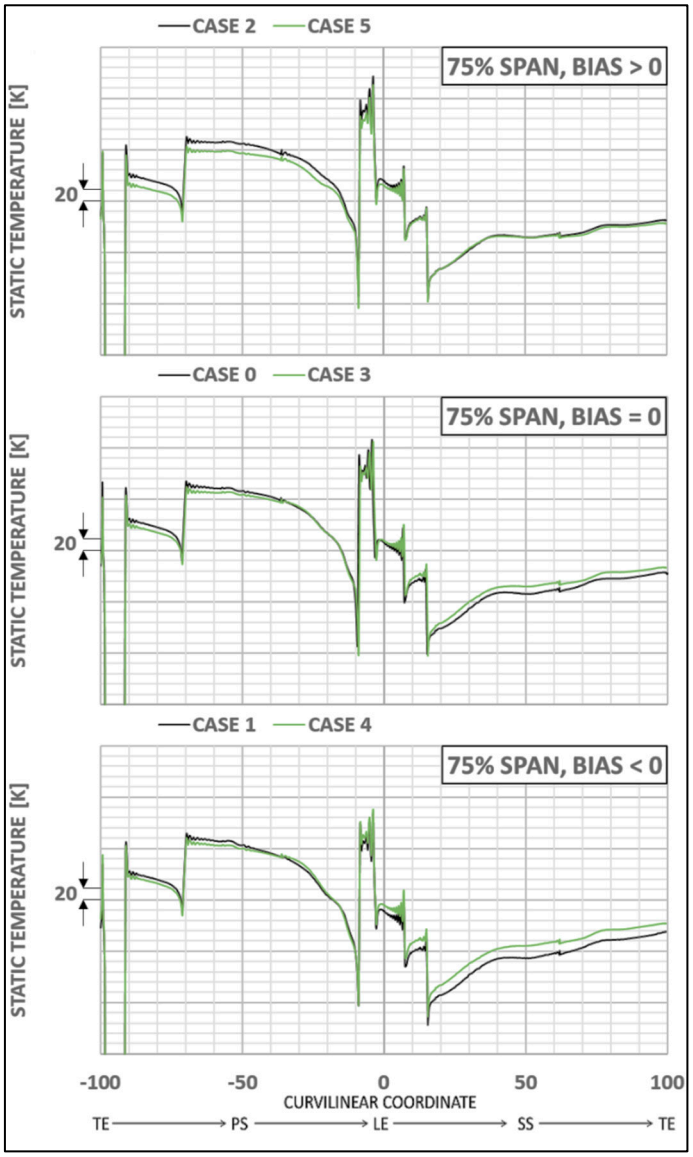

Figure 11. External CFD, near-wall gas static temperatures on the HPR surface at 75% span at constant bias, no clocking (cases 0, 1, 2 in black), half-pitch clocking (cases 3, 4, 5 in green) resulting from phase-lag cycle-averaged solutions, plotted as a function of the section's curvilinear co-ordinate.

Table 2 shows the non-dimensional peak near-wall gas static temperatures predicted by the model on the surfaces of each of the two HPS vanes (left vane 1, right vane 2) for the different cases. The temperatures in Table 2 have been non-dimensionalized by dividing the values by the reference peak temperature, calculated on Vane 1 for the baseline conditions (case 0). The values in Table 2 show that clocking by half-pitch has a significantly beneficial effect on peak HPS temperatures. Interestingly, for the zero-clocking case, biasing the inlet temperature field by a positive 10% promotes lower peak temperatures. This has to do with the destructive interference of the tip-biased temperature peak, traveling in close proximity to the outer end-wall when it meets the vane leading edges, with the large amount of coolant emitted by the RODN cooling holes. This tendency is not present in the clocked inlet case, as reported in Table 2, because due to the rotation of the inlet field, the temperature peaks on both vanes are formed at a lower span, outside the region that falls under RODN coolant protection.

Table 2. Peak HPS static temperatures (non-dimensional).

Clocking \ Bias	0°		θp/2	
	Vane 1	Vane 2	Vane 1	Vane 2
+10% span	0.985	0.921	0.955	0.906
0	1.000	0.925	0.945	0.900
−10% span	0.992	0.909	0.932	0.886

In summary, it appears that a half-pitch clocking can help alleviate peak temperatures on the HPS, with negligibly (~5 K) higher LE temperatures on the HPR, compared to the un-clocked counterpart, when combined with a negatively biased RTD. According to these considerations, the inlet temperature distribution identified as "CASE 4" corresponds to the best performing one. This inlet field leads to achieve 45 K lower peak temperatures on the HPR surface and a 6.8% reduction in peak HPS temperatures. However, it must be noted that an undesirable feature of all the cases analyzed up to this point is the fact (as shown in Table 2) that the two stator vanes are experiencing vast differences in individual peak temperatures. This may create problems on multiple fronts, including structurally due to differential thermal stresses and deformations on the HPS interfaces with the casings and combustor, and thermodynamically, because of the need to design an oversized cooling system only to provide enough coolant for the higher-temperature vane.

3.3. Optimized Inlet Temperature Field

Based on the considerations derived from the results of the previous sections, a new inlet temperature distribution with negative bias and "enhanced circumferential uniformity" (ECU) traverse is conceived. This was done with the help of a specialized team in Rolls-Royce plc, who provided the results from a combustion LES. From this simulation, the resulting time-average temperature field at an axial position corresponding to the "MAIN INLET" of Figure 1 was extracted to be used as a BC for the model. Figure 12 shows the new BC (A) in comparison with the best performing parametric one (B) which, as previously mentioned, was identified with the one listed as CASE 4. The ECU distribution was conceived around the need for having the highest possible amount of hub bias and a circumferentially mixed temperature field devoid of localized hot regions.

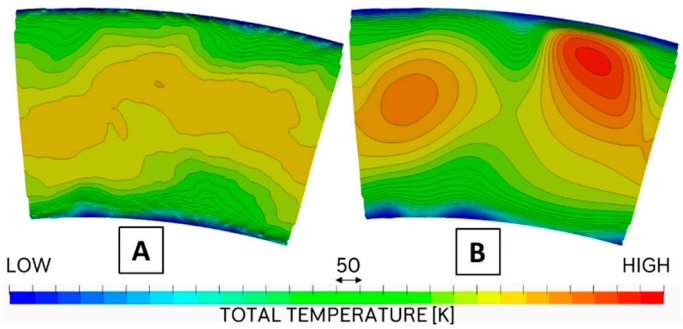

Figure 12. Total temperature contours at the HPS inlet corresponding to the new optimized ECU distribution (**A**) versus the best-performing parametric one, i.e., CASE 4 (**B**)—pictures distorted.

This was obtained through iterative matching aimed at providing the same amount of energy as the baseline and parametric cases analyzed in the previous sections. The energy content was evaluated based on the mass-weighted total temperature integral of the RTD curve over the whole span. A comparison between the two HPS inlet circumferentially averaged radial distributions can be seen in Figure 13A. The ECU RTD represented by the purple curve in Figure 13A appears to have a marked hub bias. In terms of traverse migration, Figure 13B and Figure 13C, respectively, show the RTDs at HPS exit and HPR

exit. The effect of hub bias can be still seen at these axial stations, while in the upper portion of the span the ECU traverse leaves the HPR row with slightly higher temperatures (see Figure 13C for 0.8 < SPAN < 1.0). This effect is already present at the HPS exit (Figure 13B) in the higher fifth of the span, where the pink curve presents higher values than the black one, although this is less evident due to the high slope of the curves in that region.

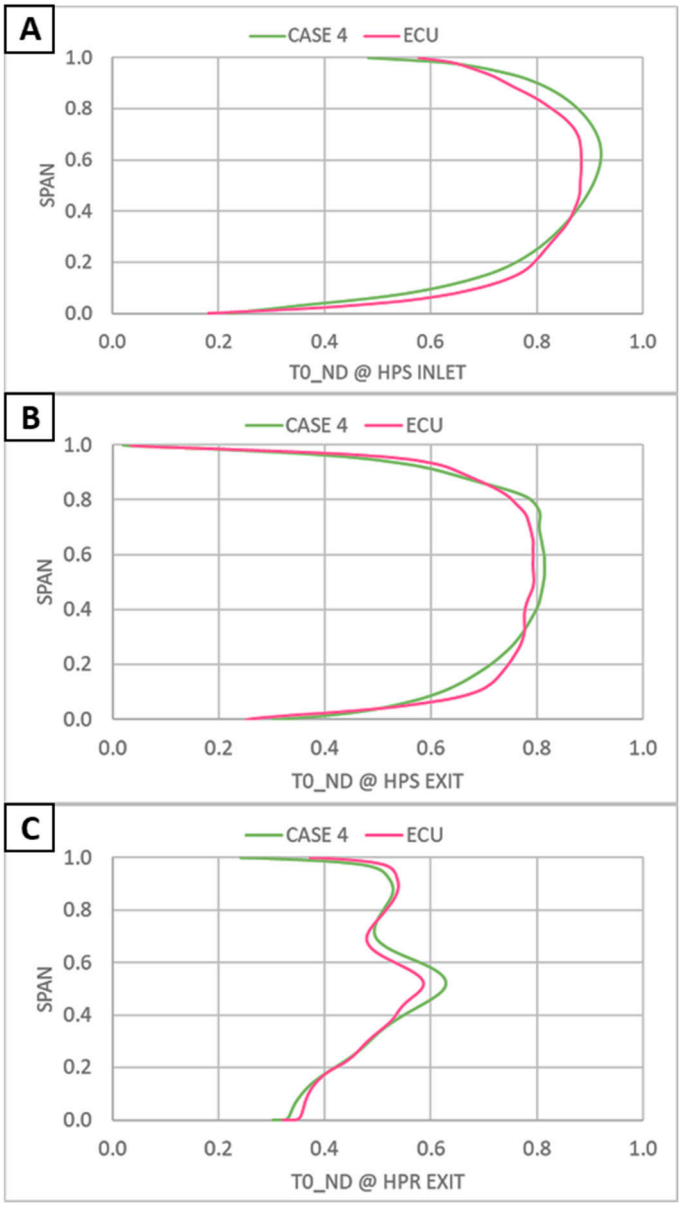

Figure 13. RTDs at the HPS main inlet for the CASE 4 and ECU cases in terms of non-dimensional total temperatures ($T0_{\_ND}$) as a function of span, at the HPS Inlet (**A**), HPS Exit (**B**) and HPR Exit (**C**)—CASE 4 distribution (green) and ECU distribution (purple).

The migration of the two inlet fields is also studied in terms of HPR surface adiabatic recovery temperatures for the same three constant-span sections used previously. This is shown in Figure 14, where it is in interesting to see that the optimized ECU traverse provides a significantly more uniform temperature profile throughout the section, when compared to the best performing parametric traverse. The latter was already achieving good results in terms of peak temperatures and uniformity with respect to the baseline, as previously shown. This translates into lower maximum temperatures, which is clearly visible in the LE region at 75% span, and smaller temperature gradients across the different

sections of the blades. However, this also means that the suction side of the blade, which is mostly unprotected in terms of film cooling, is now experiencing higher near-wall gas temperatures. This is a topic for a further multi-disciplinary evaluation.

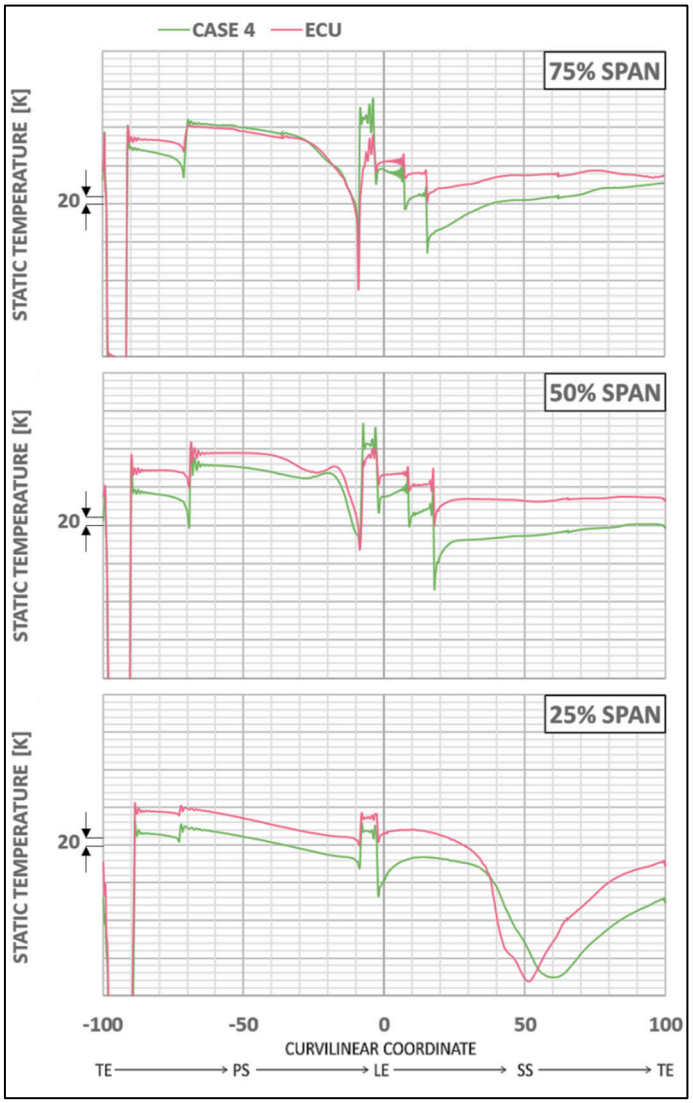

Figure 14. External CFD, near-wall gas static temperatures on the HPR surface for CASE 4 (green) and ECU (purple) at three constant-span sections resulting from phase-lag cycle-averaged solutions, plotted as a function of the section's curvilinear co-ordinate.

A comparison was carried out between the ECU traverse and the best performing parametric traverse of CASE 4 in terms of non-dimensional (divided by the peak HPS temperature on vane 1 for case 0) peak near-wall gas static temperatures on the HPS surface. This comparison is reported in Table 3. As reported in Table 3, the new ECU traverse provides lower peak HPS temperatures with much more uniform values in terms of differences between the two stator vanes.

Table 3. Peak HPS static temp. (non-dimensional), II.

CASE ID	Vane 1	Vane 2
CASE 4	0.932	0.886
ECU	0.925	0.910

In summary, the circumferentially uniform traverse performs better than any of the parametric ones, for both high-pressure turbine rows with ~100 K lower peak temperatures on the HPR surface and a significant 7.5% peak temperature reduction on the HPS one.

4. Conclusions

The high-pressure turbine of a modern turbofan engine represents the most thermally stressed part of the machine. In the continuous effort aimed at achieving additional points of thermodynamic cycle efficiency, the temperatures in this part of the engine have been increasing since the start of the jet engine era. In many cases, relatively large amounts of thermal energy are localized in confined, small regions of the turbine inlet flow-field. During the migration through the high-pressure stage, these high-temperature streams are also characterized by peculiar behaviors such as segregation that cause them to persistently impinge on the same portions of the high-pressure rotor surface, promoting overheating and erosion. By rearranging the inlet temperature field both in the circumferential and radial directions, this behavior can be modified in order to mitigate the above-mentioned detrimental effects. This work has been focused on parametrizing the position of the high-temperature regions in the turbine inlet flow-field and evaluating the effects of these parametric modifications on the maximum high-pressure stator and high-pressure rotor temperatures.

This investigation was carried out numerically, using three-dimensional unsteady (phase-lag) simulations and steady-state conjugate heat transfer simulations on a modern high-pressure turbine geometry. Through this parametrization, an optimal combination of circumferential and radial shifting of the inlet flow-field was identified, capable of providing 45 K lower peak static temperatures on the high-pressure rotor, and a 6.8% reduction in the maximum surface static temperatures on the high-pressure stator. The findings from the parametric analysis allowed the definition of the requirements for a novel, circumferentially mixed inlet temperature profile, which was created in Rolls-Royce plc through combustion LES. The new inlet distribution was tested on the current setup and achieved a remarkable 100 K reduction in high-pressure rotor peak surface static temperatures, in conjunction with 7.5% lower peak temperatures on the high-pressure stator vanes.

Furthermore, when compared to the best-performing parametric traverse, the optimized one allows for a significantly more uniform heat load allocation on the stator vanes. An additional comparative analysis was carried out on the predictions provided by steady-state and phase-lag models in terms of surface rotor temperatures for three cases with different radial bias of the inlet distribution. The authors found that the global maximum temperatures registered on the leading edge at the highest span section are not noticeably dependent on the modelling technique. On the contrary, the temperatures predicted on the rotor's pressure side by the steady-state model are significantly lower than the phase-lag counterparts, pointing to an insufficient accuracy of the former. Nevertheless, the deltas in temperature due to the boundary condition variation are still sufficiently well predicted by the steady-state model, indicating that this kind of modelling can still be used for a preliminary evaluation of the effects of radial bias.

The modelling and simulation of complex cases such as the high-pressure turbine of a modern jet engine are always associated with a trade-off between computational cost and accuracy. In the authors' view, this is especially true in industry when it comes to engine components' design, and even more so for optimization. In this work, we reported and discussed the results found by using different computational models, each associated with a different cost and fidelity level. The study indicates that the lower-fidelity and lower-cost adiabatic model can be used to drive an optimization, but it is advisable to then verify the optimum performance with a higher-fidelity conjugate simulation.

In summary:

- Clocking and biasing are powerful tools that can be employed to lower peak temperatures on the high-pressure turbine stators and rotors, downstream of a can-type combustor;
- This work, conducted on real engine geometries and boundary conditions, shows that reductions of the order of tens of kelvins can be achieved, which can have significant effects on the service life of the components;
- Aiming for a better circumferential uniformity of the inlet temperature field is even more beneficial, as shown in the present study where a peak rotor temperature reduction of a hundred kelvins was achieved. This type of inlet distribution can be generated by implementing a lean-burn combustion system.

Author Contributions: Conceptualization, M.C. and S.S.; methodology, M.C.; software, S.S.; validation, M.C. and S.S.; formal analysis, M.C.; investigation, M.C.; resources, S.S. and T.G.; data curation, M.C.; writing—original draft preparation, M.C.; writing—review and editing, M.C. and F.L.; visualization, M.C. and F.L.; supervision, S.S. and T.G.; project administration, S.S. and T.G.; funding acquisition, S.S. and T.G. All authors have read and agreed to the published version of the manuscript.

Funding: This work was conducted within the framework of the NEXTAIR project. The NEXTAIR project received funding from the European Union's Horizon Europe research and innovation program under grant agreement No 101056732.

Data Availability Statement: The authors cannot make the data available due to industrial confidentiality reasons.

Acknowledgments: The authors would like to thank Rolls-Royce plc for their support and permission to publish this work. This work has been conducted within the framework of the NEXTAIR project. Views and opinions expressed are, however, those of the author(s) only and do not necessarily reflect those of the European Union. Neither the European Union nor the granting authority can be held responsible for them.

Conflicts of Interest: Author Shahrokh Shahpar was employed by the company Rolls-Royce Plc. The remaining authors declare that the research was conducted in the absence of any commercial or financial relationships that could be construed as a potential conflict of interest.

Nomenclature

BC	Boundary condition
CFL	Courant-Friedrichs-Lewy number
CHT	Conjugate heat transfer
CSD	Casing cooling downstream to rotor blade
CSF	Casing cooling upstream to rotor blade
DSH	Hub cavity inflow downstream to rotor blade
ECU	Enhanced circumferential uniformity
FC	Rotor film cooling inlet
HPR	High-pressure rotor
HPS	High-pressure stator
HPT	High-pressure turbine
HTEC, ITEC	HPS and IPS trailing edge cooling slots
IPS	Intermediate-pressure stator
LE, TE	Leading edge, trailing edge
Φ	Cycle phase during a phase-lag simulation
PS, SS	Pressure side, suction side
RANS	Reynolds-averaged Navier-Stokes
RTD	Radial temperature distribution
RIDN, RODN	Inner and outer end-wall HPS film cooling
T0	Total temperature
$T0_{\_ND}$	Non-dimensional total temperature
θ_p	HPS periodicity angle
USH	Hub cavity inflow upstream to rotor blade

References

1. Rolls-Royce PLC. *The Jet Engine*, 5th ed.; Wiley: Chichester, UK, 2015.
2. Han, J.; Wright, L.M. 4.2.2.2 Enhanced Internal Cooling of Turbine Blades and Vanes. In *The Gas Turbine Handbook*; NETL: Morgantown, WV, USA, 2006.
3. Cunha, F.J. 4.4 Heat Transfer Analysis. In *The Gas Turbine Handbook*; NETL: Morgantown, WV, USA, 2006.
4. Harvey, N.W. Aerothermal Implications of shroudless and shrouded blades. In *VKI LS 2004-02, Turbine Blade Tip Design and Tip Clearance Treatment*; von Karman Institute for Fluid Dynamics: Rhode-St-Genese, Belgium, 2004; ISBN 2-930389-51-6.
5. Ruffles, P.C. Evolution of the Aero Gas Turbine. In *Trenchard Lecture*; Cambridge University Press: Cambridge, UK, 1991.
6. Bunker, R.S. Integration of New Aero-Thermal and Combustion Technologies with Long-Term Design Philosophies for Gas Turbine Engines. In Proceedings of the US–Ukrainian Workshop on Innovative Combustion and Aerothermal Technologies in Energy and Power Systems, Kiev, Ukraine, 21–26 May 2001.
7. Zhang, R.; Liu, P.; Zhang, X.; Xi, W.; Liu, J. Recent Developments in the Aerodynamic Heat Transfer and Cooling Technology of Gas Turbines Endwalls. *Aerospace* **2023**, *10*, 702. [CrossRef]
8. Zheng, F.; Sun, R.; Chen, Z.; Liu, Y.; Yang, W. Study on Heat Transfer Characteristics of Jet Impingement of Turbine Bending Surface. *Aerospace* **2024**, *11*, 554. [CrossRef]
9. Liu, J.; Xu, M.; Xi, W. Effects of Gas Thermophysical Properties on the Full-Range Endwall Film Cooling of a Turbine Vane. *Aerospace* **2023**, *10*, 592. [CrossRef]
10. Dorney, D.J.; Gundy-Burlet, K.L.; Sondak, D.L. Survey of Hot Streaks Experiments and Simulations. *Int. J. Turbo Ket Engines* **1999**, *16*, 1–15. [CrossRef]
11. Shang, T.; Epstein, A. Analysis of Hot Streak Effects on Turbine Rotor Heat Load. *ASME J. Turbomach.* **1997**, *122*, 544–553. [CrossRef]
12. Glezer, B. Thermal-mechanical design factors affecting turbine blade tip clearance. In *VKI LS 2004-02, Turbine Blade Tip Design and Tip Clearance Treatment*; von Karman Institute for Fluid Dynamics: Rhode-St-Genese, Belgium, 2004; pp. 1–23, ISBN 2-930389-51-6.
13. Jarrett, A.; Erukulla, V.V.; Koul, A.K. Untwist Creep Analysis of Gas Turbine First Stage Blade. In Proceedings of the ASME Turbo Expo: Turbomachinery Technical Conference and Exposition, Phoenix, AZ, USA, 17–21 June 2019. GT2019-90979.
14. Kolagar, A.M.; Tabrizi, N.; Cheraghzadeh, M.; Shahriari, M.S. Failure Analysis of Gas Turbine First Stage Blade Made of Nickel-Based Superalloy. *Case Stud. Eng. Fail. Anal.* **2017**, *8*, 71–78. [CrossRef]
15. Guo, X.; Zheng, W.; Xiao, C.; Li, L.; Antonov, S.; Zheng, Y.; Feng, Q.C. Evaluation of microstructural degradation in a failed gas turbine blade due to overheating. *Eng. Fail. Anal.* **2019**, *103*, 308–318. [CrossRef]
16. Han, J.; Dutta, S.; Ekkad, S. *Gas Turbine Heat Transfer and Cooling Technology*; Taylor & Francis: London, UK, 2000.
17. Eliaz, N.; Shemesh, G.; Latanision, R.M. Hot Corrosion in Gas Turbine Components. *Eng. Fail. Anal.* **2002**, *9*, 31–43. [CrossRef]
18. Stringer, J. High-Temperature Corrosion of Superalloys. *Mater. Sci. Technol.* **1987**, *3*, 482–493. [CrossRef]
19. Carta, M.; Ghisu, T.; Shahpar, S. High-Fidelity CFD Analysis of In-Serviced Shrouded High-Pressure Turbine Rotor Blades—TURBO-22-1122. *ASME J. Turbomach.* **2022**, *144*, 121001. [CrossRef]
20. Virdis, I.; Ghisu, T.; Shahpar, S.; De La Puerta, I.; Li, H. Digital Shadow and Robust Optimization of In Service Squealer Tip Turbine Blades. In Proceedings of the Asme Turbo Expo, Rotterdam, The Netherlands, 13–17 June 2022.
21. Busby, J.; Sondak, D.; Staubach, B.; Davis, R. *Deterministic Stress Modeling of Hot Gas Segregation in a Turbine*; NASA Technical Report UTRC 98-07; NASA, Lewis Research Center: Cleveland, OH, USA, 1998.
22. Butler, T.L.; Sharma, O.P.; Joslyn, H.D.; Dring, R.P. Redistribution of an Inlet Temperature Distortion in an Axial Flow Turbine Stage. *J. Propuls. Power* **1989**, *5*, 64–71. [CrossRef]
23. Kerrebrock, J.; Mikolajczac, A. Intra-Stator Transport of Rotor Wakes and Its Effect on Compressor Performance. *ASME J. Eng. Power* **1970**, *92*, 359–368. [CrossRef]
24. Rai, M.M.; Dring, R.P. Navier-Stokes Analyses of the Redistribution of Inlet Temperature Distorsions in a Turbine. *J. Propuls. Power* **1990**, *6*, 276–282. [CrossRef]
25. Dorney, D.J.; Davis, R.L.; Edwards, D.E. Unsteady Analysis of Hot Streak Migration in a Turbine Stage. *J. Propuls. Power* **1992**, *8*, 520–529. [CrossRef]
26. Takahashi, R.; Ni, R.H. Unsteady Hot Streak Simulation through 1 1/2 Stage Turbine. In Proceedings of the AIAA, SAE, ASME, and ASEE, 27th Joint Propulsion Conference, Sacramento, CA, USA, 24–26 June 1991; p. 3382.
27. Dorney, D.J.; Davis, R.; Edwards, D.; Madavan, N. Effects of Tip Clearance on Hot Streak Migration in a High-Subsonic Single-Stage Turbine. *J. Turbomach.* **2000**, *122*, 613–620. [CrossRef]
28. Jiang, H.; Peng, X.; Xie, W.; Lu, S.; Gu, Y. Development of a Large-Scale High-Speed Linear Cascade Rig for Turbine Blade Tip Heat Transfer Study. *Aerospace* **2022**, *9*, 695. [CrossRef]
29. Caloni, S.; Shahpar, S.; Toropov, V. Multi-Disciplinary Design Optimisation of the Cooled Squealer Tip for High Pressure Turbines. *Aerospace* **2018**, *5*, 116. [CrossRef]
30. Yan, D.; Jiang, H.; Li, J.; Xie, W.; Wang, Z.; Lu, S.; Zhang, Q. Influence of Gas-to-Wall Temperature Ratio on the Leakage Flow and Cooling Performance of a Turbine Squealer Tip. *Aerospace* **2022**, *9*, 627. [CrossRef]
31. Basol, A.M.; Jenny, P.; Ibrahim, M.; Kalfas, A.I.; Abhari, R.S. Hot Streak Migration in a Turbine Stage: Integrated Design to Improve Aerothermal Performance. *J. Eng. Gas Turbines Power* **2011**, *133*, 061901-1. [CrossRef]

32. Bunker, R. *Advances in Turbomachinery Aero-Thermo-Mechanical Design Analysis*; VKI LS, Von Karman Institute Lecture Series 2007-02; GE Global Research: Niskayuna, NY, USA, 2007.
33. Carta, M.; Ghisu, T.; Shahpar, S. Heat Transfer Analysis of Damaged Shrouded High-Pressure Turbine Rotor Blades. *Int. J. Turbomach. Propuls. Power* **2023**, *8*, 24. [CrossRef]
34. Dorney, D.; Burlet, K. Hot Streak Clocking in a 1-1/2 Stage Turbine. *J. Propuls. Power* **1996**, *12*, 619–620. [CrossRef]
35. An, B.; Liu, J.; Jiang, H. Numerical Investigation on Unsteady Effects of Hot Streak on Flow and Heat Transfer in a Turbine Stage. *J. Turbomach.* **2009**, *131*, 031015. [CrossRef]
36. HE, L.; Menshikova, V.; Haller, B.R. Influence of Hot Streak Circumferential Length-Scale in Transonic Turbine Stage. In Proceedings of the ASME Turbo Expo, Vienna, Austria, 14–17 June 2004.
37. Zhang, S.; Ding, S.; Liu, P.; Qiu, T. Effect of Hot Streak on Aerothermal Performance of High Pressure Turbine Guide Vane under Different Swirl Intensities. *Aerospace* **2022**, *9*, 579. [CrossRef]
38. Yang, X.; Cai, H.; Kang, J.; Liu, W.; Li, P. Influence of Hot Streak and Swirl Clocking Position on Aerothermal Performance of High-Pressure Turbine. *Aerospace* **2023**, *10*, 934. [CrossRef]
39. Michelassi, V.; Giangiacomo, P.; Martelli, F.; Dénos, R.; Paniagua, G. Steady Three-Dimensional Simulation of a Transonic Axial Turbine Stage. In Proceedings of the ASME Turbo Expo 2001, New Orleans, LA, USA, 4–7 June 2001.
40. Adamczyk, J.J.; Mulac, R.A.; Celestina, M.L. A Model for Closing the Inviscid Form of the Average-Passage Equation System. *J. Turbomach.* **1986**, *108*, 180–186. [CrossRef]
41. Turner, M.G.; Vitt, P.H.; Topp, D.A.; Saeidi, S.; Hunter, S.D.; Dailey, L.D.; Beach, T.A. Multistage Simulations of the GE90 Turbine. In Proceedings of the 1999 International Gas Turbine and Aeroengine Congress, Indianapolis, IN, USA, 7–10 June 1999.
42. Praisner, T.J.; Magowan, J.W.; Clark, J.P. Predictions of Temperature Redistribution in a Turning Duct and in High-Pressure Turbines, GT2003-38317. In Proceedings of the ASME Turbo Expo 2003, Atlanta, GA, USA, 16–19 June 2003.
43. Carta, M.; Ghisu, T.; Shahpar, S. Multi-Fidelity Heat Transfer Analysis of Shrouded High-Pressure Turbine Rotor Blades. In Proceedings of the ASME Turbo Expo 2023, Boston, MA, USA, 26–30 June 2023.
44. Deng, Q.; Wang, H.; He, W.; Feng, Z. Cooling Characteristic of a Wall Jet for Suppressing Crossflow Effect under Conjugate Heat Transfer Condition. *Aerospace* **2022**, *9*, 29. [CrossRef]
45. Demargne, A.A.J.; Evans, R.O.; Tiller, P.J.; Dawes, W.N. Practical and Reliable Mesh Generation for Complex, Real-World Geometries. In Proceedings of the AIAA 52nd Aerospace Sciences Meeting, National Harbor, MD, USA, 13–17 January 2014.
46. Shahpar, S.; Lapworth, L. PADRAM: Parametric Design and Rapid Meshing System for Turbomachinery Optimisation, GT2003-38698. In Proceedings of the ASME Turbo Expo and International Joint Power Generation Conference, Atlanta, GA, USA, 16–19 June 2003; pp. 579–590.
47. Lapworth, L. Hydra CFD: A Framework for Collaborative CFD Development. In Proceedings of the International Conference on Scientific and Engineering Computation (IC-SEC), Singapore, 30 June–2 July 2004.
48. Castillon, L. Evaluation of a multiple frequency phase lagged method for unsteady numerical simulations of multistage turbomachinery. In Proceedings of the 28th Congress of the International Council of the Aeronautical Sciences ICAS 2012, Brisbane, Australia, 23–28 September 2012; Volume 4, pp. 2581–2592.
49. Carta, M.; Shahpar, S.; Ghisu, T. Analysis of the aerothermal performance of modern commercial high-pressure turbine rotors using different levels of fidelity. *Proc. Inst. Mech. Eng. Part A J. Power Energy* **2024**. [CrossRef]

Disclaimer/Publisher's Note: The statements, opinions and data contained in all publications are solely those of the individual author(s) and contributor(s) and not of MDPI and/or the editor(s). MDPI and/or the editor(s) disclaim responsibility for any injury to people or property resulting from any ideas, methods, instructions or products referred to in the content.